Instability and Transition Experiments in the Boeing/AFOSR Mach 6 Quiet Tunnel

Gregory R. McKiernan,* Brandon C. Chynoweth,* Josh B. Edelman,* J. Adam McKenzie,*
Cameron J. Sweeney,* and Steven P. Schneider[†]
School of Aeronautics and Astronautics
Purdue University
West Lafayette, IN 47907-1282

This paper presents results for three projects in the Boeing/AFOSR Mach 6 Quiet Tunnel (BAM6QT) at Purdue University. The second-mode instability was measured on a straight $3°$ half-angle cone under quiet conditions using pressure sensors and temperature sensitive paint. Natural transition was observed near the aft end of the model at a unit Reynolds of 12.1×10^6/m. Maximum pressure fluctuation magnitudes prior to the onset of transition were measured to be 27% of the mean surface pressure. Secondly, experiments on a $7°$ half-angle cone at $6°$ angle of attack were performed to verify the presence of a secondary instability of a stationary crossflow wave. Using TSP imaging techniques and PCB pressure transducers, a possible secondary instability with a peak frequency near 300 kHz was measured at azimuthal angles between $125°$ and $140°$ at Reynolds numbers near 10.7×10^6/m. Lastly, Roughness elements and an air jet were tested as boundary layer trips on a generic hypersonic forebody.

Nomenclature

f	frequency		T	Temperature
M	Mach number		t	time
p	pressure		x	model axial coordinate
$\dot{q}$	heat flux		y	model spanwise coordinate
Re	Reynolds number			

Subscripts

0	stagnation condition
$wall$	wall condition
∞	freestream condition

Abbreviations

BAM6QT	Boeing/AFOSR Mach-6 Quiet Tunnel
TSP	Temperature-Sensitive Paint
PSD	Power-Spectral Density
RIM	Rod Insertion Method
SB	Schmidt-Boelter

---

*Research Assistant. Student Member, AIAA
[†]Professor. Associate Fellow, AIAA

I.   Introduction

A.   Hypersonic Laminar-Turbulent Transition

Predicting laminar to turbulent transition of hypersonic boundary layers is vitally important for designing high speed vehicles, but the underlying physics that cause this transition are poorly understood. Hypersonic boundary-layer transition affects heat transfer, skin friction, separation and other boundary layer properties. If transition could be accurately predicted then future hypersonic vehicle designs could be more efficient and accurate. Conventional hypersonic tunnels have noise levels between 1-4%. These noise levels will cause transition to occur earlier than in quiet flow and can be more than an order of magnitude greater than in flight. Quiet wind tunnels produce freestream noise levels of less than 0.1% and provide test conditions that can be used to study laminar-turbulent transition at noise levels similar to flight. Transition mechanisms present in low noise environments can be changed or missed in high-noise environments.

B.   The Boeing/AFOSR Mach-6 Quiet Tunnel

The Boeing/AFOSR Mach-6 Quiet Tunnel (BAM6QT), shown in Figure 1, is the largest operational hypersonic quiet wind tunnel in the world. The BAM6QT is a Ludweig tube design incorporating a long driver tube with a converging-diverging nozzle at the downstream end. Tunnel operation consists of filling the driver tube section to the desired pressure and pumping down a vacuum tank. A pair of diaphragms is then burst causing an expansion fan to propagate upstream. The expansion fan reflects between the end of the driver tube and the contraction section. These expansion wave produces a quasi-static drop in stagnation pressure of about 1% per reflection throughout the run.
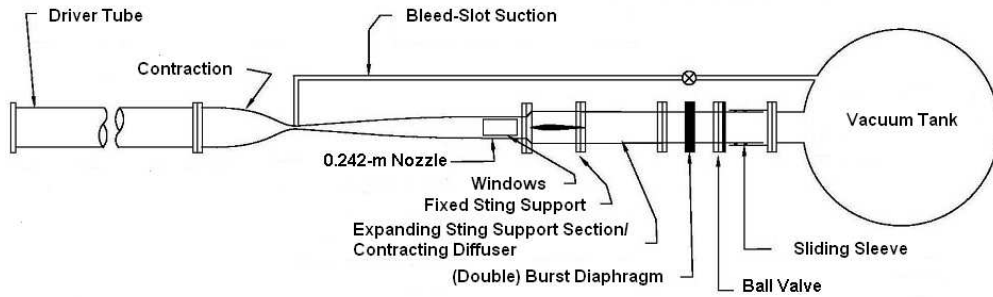

Figure 1. Schematic of Boeing/AFOSR Mach 6 Quiet Tunnel.

The BAM6QT is able to produce noise levels on the order of 0.05% for unit Reynolds numbers of approximately $12.7{\times}10^6$/m. The BAM6QT employs several features to produce a high quality low noise environment. The diverging section of the nozzle is polished to a mirror finish to avoid nozzle wall roughness disturbing the boundary layer. Additionally, the driver tube air is passed through very fine air filters to remove any particles that could damage the mirror finish. The divergent portion is very long to reduce the effect of the Görtler instability. Lastly, a suction slot upstream of the throat can be opened to the vacuum tank in order to remove the boundary layer from the nozzle wall. This allows a fresh laminar boundary layer to begin at the throat. If the suction slot is not used the BAM6QT can operate with noise levels near 3%. This noise level is typical of conventional hypersonic wind tunnels.

II.   Transition Measurements on a Straight 3° Half-Angle Cone

Current hypersonic laminar-turbulent transition prediction methods rely on semi-empirical relationships. Those such as e^N are based on the linear growth of an instability but cannot take into account freestream noise levels, non-linear growth, breakdown, and complex interactions between instability types.[1] It is therefore necessary to develop a mechanism-based prediction method that incorporates more of the underlying physics of the transition process. The second-mode instability, which dominates for axisymmetric models at zero angle of attack, can be experimentally measured with pressure sensors.[2] Correlation of the pressure fluctuation magnitudes to the beginning of transition may lead to more reliable methods for hypersonic vehicle design and optimization.[3]

Experiments at Purdue University to understand the physics of transition due to second-mode waves have centered around using a flared-cone geometry at zero angle of attack. While the flared cone provides a platform for the creation of large amplitude second-mode waves, the concave shape promotes growth of the Görtler instability. Under quiet flow, streaks of heating form in a unique pattern as shown in Figure 2. Each region of increased heat transfer is composed of many individual streaks that form around the circumference of the model. The most unique feature is the two regions of increased heating near 43 and 52 cm from the nosetip that are separated by a cooler region. Maximum pressure fluctuation magnitudes due to the second-mode instability are normally between 25-30% of the surface static pressure.[4]
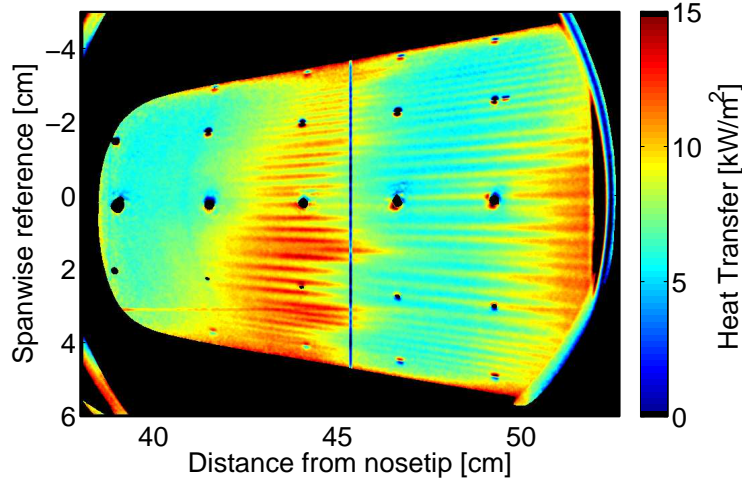

Figure 2. TSP image of the Purdue flared cone geometry at a unit Re = 9.2×10^6/m from Reference 4. Flow is from left to right.

Experiments performed by Sebastian Willems on a straight 3° half-angle cone in the BAM6QT facility in 2012 indicated that transition due to the second-mode instability had occurred.[5] Until these experiments, natural transition due to the second mode had not been observed on a straight walled cone under quiet flow. Pressure fluctuation data at a unit Reynolds of 12.7×10^6/m showed the growth of second-mode waves as well as a broadband increase in noise normally observed in transitional and turbulent boundary layers. The current author attempted to duplicate and expand on the results of Willems. Pressure fluctuation and temperature sensitive paint measurements were conducted to compare the transition process on a straight cone versus the previous results from the flared cone.

3

A. Model and Instrumentation

The 3° half-angle cone fabricated at Purdue University is composed of two pieces, a nosetip and a frustum, resulting in a total model length of 94.6 cm. The extreme length of the model and the need to image the temperature sensitive paint (TSP) applied to the aft end of the model, resulted in the nosetip being just 1.52 m from the throat. Centerline Mach number distributions computed by Schneider indicate that the Mach number at the nosetip is 5.8 which is near the 6.0 of the uniform flow farther aft. The nose was made as nearly sharp as was feasible. Two measurements of the nosetip radius were performed using a Zygo ZeGage optical surface profiler and a microscope equipped with a Moticam 3.0 mega-pixel camera. The average nosetip radius was 80 μm.

Sensor holes with a diameter of 3.2 mm were drilled perpendicular to the model surface to accommodate the installation of either PCB132A31 pressure sensors or Medtherm Schmidt-Boelter heat transfer gauges. Five holes were placed along a single ray at axial distances of 767, 813, 857, 902, and 939 mm from the nosetip as shown in Figure 3. Two additional sensor holes were added +/- 120° away from the main sensor ray at the 767 mm location to assess the precision to which the model could be placed at zero angle of attack. The position of the sensors located off the main ray are defined in Figure 3.
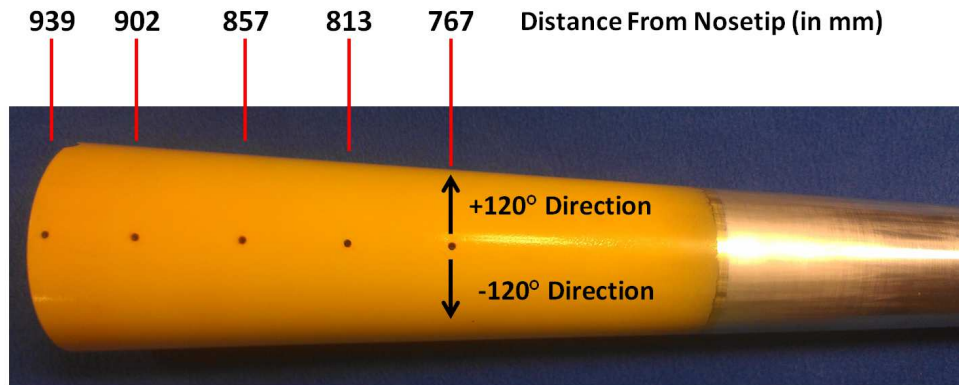

Figure 3. Photograph of 3° half-angle cone with sensor positions marked for reference in TSP images.

All PCB132A31 data were collected at a rate of 5 MHz. Power spectral densities were calculated using Welch's method. A 0.1 second long portion of data was processed with 50% overlap between windows. For a desired frequency resolution of 2 kHz, this resulted in 2500 points per window. Pressure fluctuation data were normalized by the mean static pressure on the model surface as determined using a Taylor-Maccoll solver and isentropic relationships for compressible flow.

B. Angle-of-Attack Adjustment

When an axisymmetric model is at zero angle of attack, the boundary layer should have the same thickness around the entire circumference at any given streamwise location. Since the second-mode wave frequency is tuned to the boundary-layer thickness, the three sensors at 767 mm can be used to determine how well the model is aligned with the freestream flowfield. When properly aligned, the three PCB132A31 sensors should all measure the same second-mode frequency. Willems successfully performed alignment during his experiments with a specially designed sting that allowed for minute changes in angle of attack. Since this sting is no longer available for testing at Purdue University, it was necessary to use the less accurate set screws in the sting support section of the BAM6QT for angle-of-attack adjustments.

Experiments to assess the angle of attack were performed at a freestream unit Reynolds number of approximately 2.5×10^6/m under noisy conditions. Figure 4(a) shows the initial power spectral densities from the three sensors x = 767 mm. An instability with a frequency of approximately 85 kHz is measured by the PCB sensors on the main ray and -120° from the main ray, but no instability is measured by the

4

sensor $+120°$ from the main ray. Changes were made to the set screws in the sting support in an attempt to adjust the angle of attack. Figure 4(b) is the PSD for the same sensors after adjusting the set screws. It can be seen that altering the position of the set screws had almost no effect on the peak frequency measured at each location.
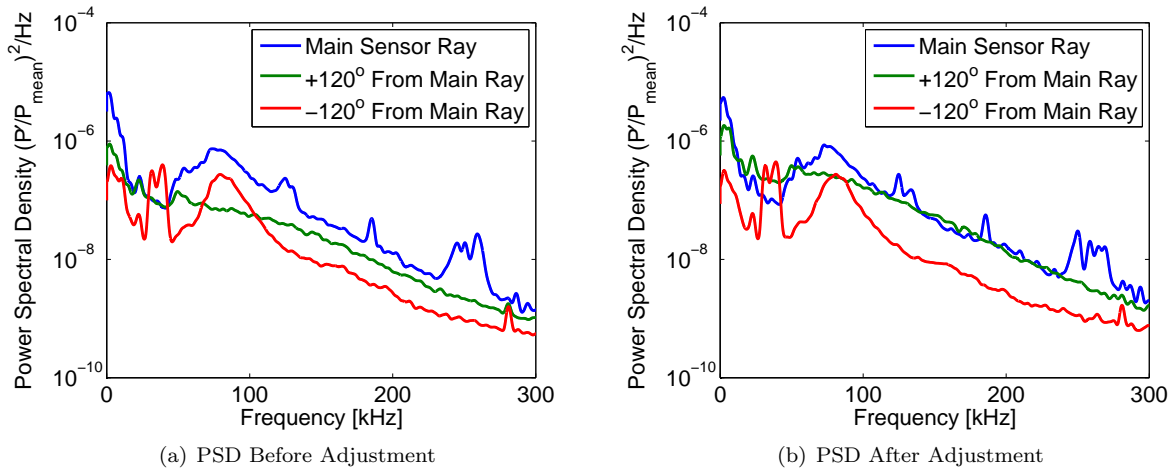

(a) PSD Before Adjustment

(b) PSD After Adjustment

Figure 4. Power spectral densities demonstrating difficulty in adjusting angle of attack to zero degrees. Noisy flow at nominal unit Reynolds number of $2.5\times10^6/\text{m}$.

The slight deviation from zero angle of attack becomes even more apparent under quiet conditions. Figure 5 shows two power spectra at unit Reynolds numbers of 10.8 and $12.0\times10^6/\text{m}$. The primary second-mode frequency is lowest on the $+120°$ ray, indicating the thickest boundary layer. Moving azimuthally towards the main ray the frequency increases, and therefore the boundary layer thins, by approximately 22%. The same phenomenon is observed at both freestream unit Reynolds numbers. In light of this result, a new sting based on drawings supplied by Sebastian Willems is currently in development for use during future tests in the BAM6QT facility.

(a) unit Re = 10.8 $\times10^6/\text{m}$
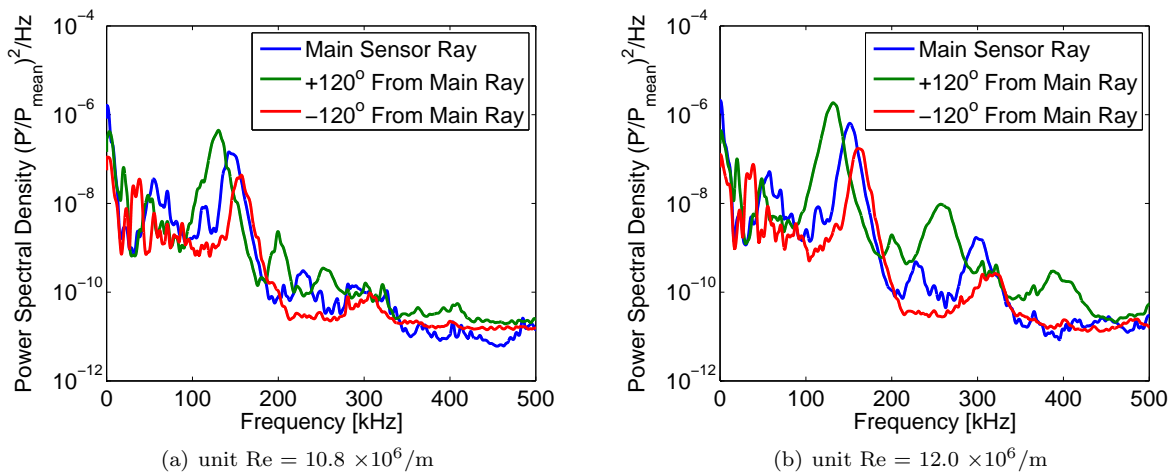
(b) unit Re = 12.0 $\times10^6/\text{m}$

Figure 5. Power spectral densities for PCB sensors around azimuth 767 mm from the nosetip under quiet flow at two different freestream unit Reynolds numbers.

5

C.   Preliminary Results

Pressure fluctuation and TSP data were collected at three freestream unit Reynolds numbers under quiet flow. Figure 6(a) shows the PSD at a unit Reynolds number of $8.2{\times}10^6$/m. A second-mode wave with a frequency of 125 kHz was measured. The peaks at 200 kHz and above are due to electrical noise as verified by data taken prior to the run. As the Reynolds number is increased to $10.8{\times}10^6$/m, a second-mode wave with a frequency of 145 kHz is first measured at x = 767 mm. As the boundary-layer thickness increases in the downstream direction, the peak second-mode frequency decreases to 135 kHz at x = 857 mm and finally to 130 kHz at x = 902 and 939 mm. The presence of harmonics indicates non-linear amplification. The boundary layer is laminar over the entire length of the cone. Looking at the TSP image at a unit Reynolds number of $10.8{\times}10^6$/m, Figure 7, it can be seen that there are no large temperature gradients as would be expected if the boundary layer was transitioning to turbulence.
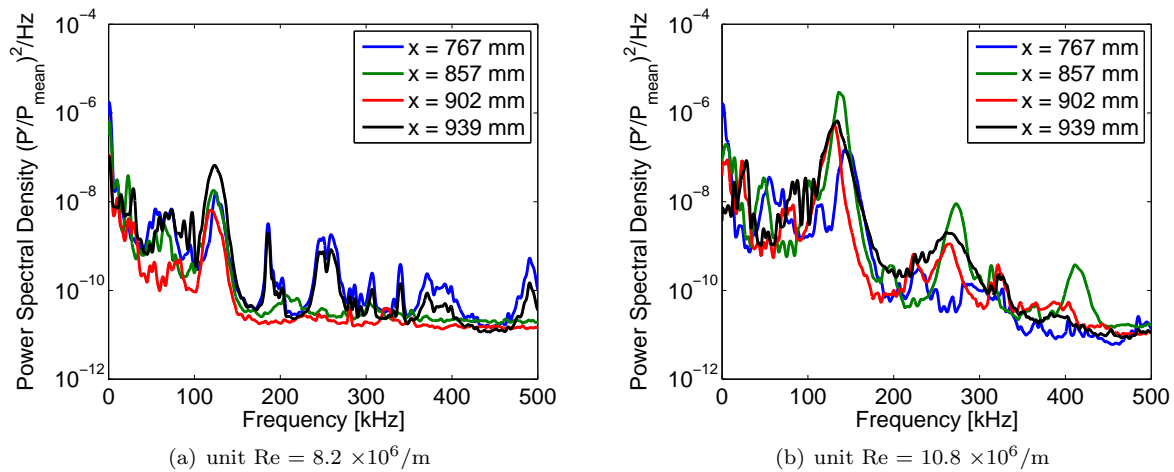

(a) unit Re = 8.2 $\times10^6$/m

(b) unit Re = 10.8 $\times10^6$/m

Figure 6. PSD from main sensor ray under quiet flow at two different freestream unit Reynolds numbers.
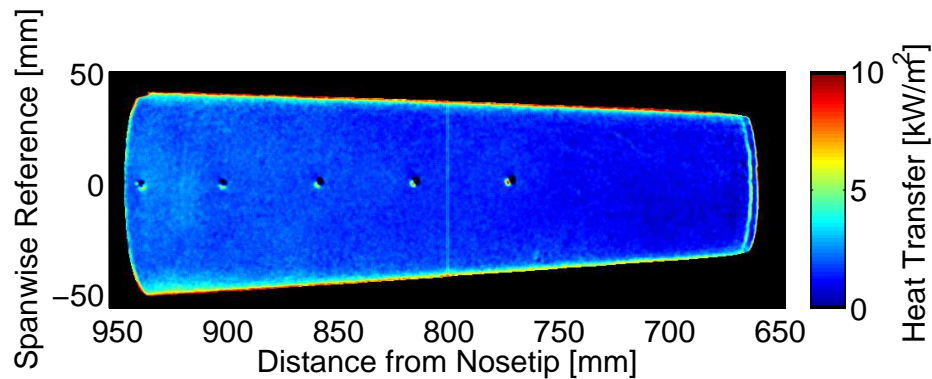

Figure 7. TSP at a unit Reynolds number of $10.8{\times}10^6$/m, quiet. Flow is from right to left.

The highest freestream Reynolds number tested was 12.1×10^6/m. The power spectra along the main sensor ray is shown in Figure 8. Additionally, a table of the pressure fluctuation magnitudes at each location is provided. Magnitudes were calculated by integrating the power spectra over a 100 kHz bandwidth centered at the peak second-mode frequency. At a distance of 767 mm from the nosetip, the peak second-mode frequency is 150 kHz. The frequency decreases to 145 kHz at x = 857 mm, and first and second harmonics are measured. Additionally, this location measures the maximum pressure fluctuation magnitude of 27.4%. This magnitude is similar to the maximum measured on the flared cone geometry.

Data from the PCB sensor at 902 mm from the nosetip show a decrease in the peak PSD amplitude and pressure fluctuation magnitude of the primary second-mode frequency. A broadband increase in signal in the power spectra indicates a transitional boundary layer. At the furthest downstream location, only the primary second-mode frequency is visible due to increasing broadband signal levels. The spectra does not appear to be fully turbulent, since signal levels for frequencies below 100 kHz have not significantly increased. A TSP image at the same unit Reynolds number is shown in Figure 9. The increase in heat transfer on the lower half of the cone starting at 900 mm from the nosetip appears to be due to transition. No streaks of heating like those on the flared cone are observed. It should be further noted that increased heat transfer is not uniform around the circumference of the model. Future testing will be continued with a new sting capable of finer adjustments to ensure the cone is closer to zero angle of attack.
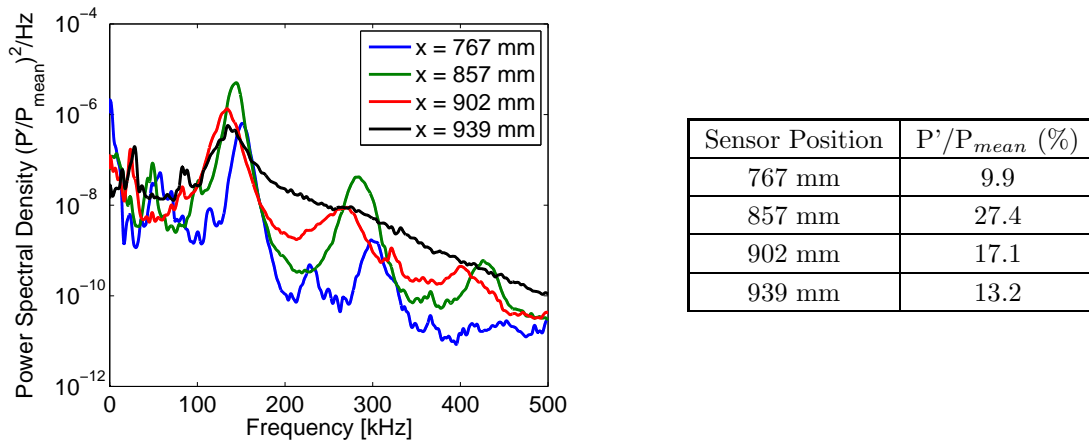

Sensor Position	P'/P$_{mean}$ (%)
767 mm	9.9
857 mm	27.4
902 mm	17.1
939 mm	13.2

Figure 8. PSD from main sensor ray under quiet at a unit Re = 12.1×10^6/m. Table indicates pressure fluctuation magnitudes from integrated power spectra.
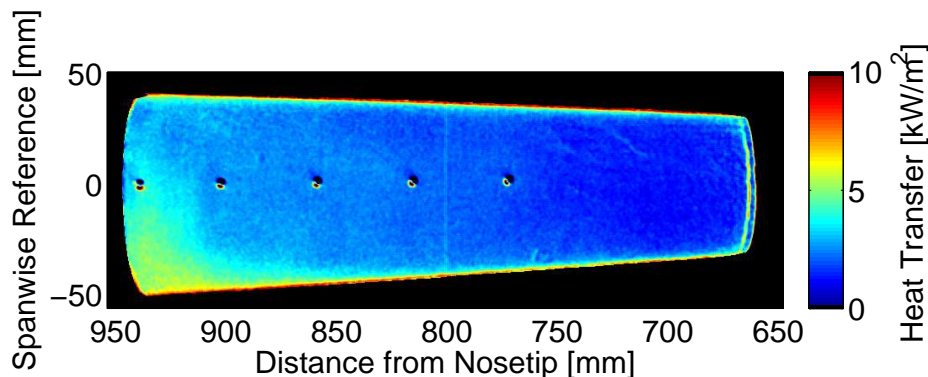

Figure 9. TSP at a unit Reynolds number of 12.1×10^6/m, quiet. Flow is from right to left.

7

III. Secondary Instability of the Stationary Crossflow Wave

A. Introduction

For a cone at angle of attack, a circumferential pressure gradient causes the streamlines to be curved towards the leeward ray. The streamwise velocity in the boundary layer decreases as the fluid approaches the wall, but the pressure gradient remains constant. This generates a secondary flow perpendicular to the streamlines, which is known as crossflow. Crossflow velocity must decrease to zero at the wall due to the no-slip condition, creating an inflection point in the crossflow velocity profile.[6] This inflection point is a source of inviscid instability and creates co-rotating vortices which can be either stationary or traveling with respect to the body.

When the stationary instability reaches saturation, a high-frequency secondary instability appears.[7] This secondary instability travels along the stationary crossflow vortices as a ring-like vortex and always appears just before the end of development of the stationary crossflow vortices.[8] The frequency of the secondary instability which develops is roughly ten times larger than the frequency of the stationary wave.[9] Previous experimentation in the BAM6QT performed by Ward and Henderson on a 7° half-angle cone at angle of attack showed possible signs of a secondary instability of the stationary crossflow wave.[10] Experiments were designed to expand on the previous experiments by Ward and Henderson with the addition of TSP to observe the secondary instability.

B. Model and Instrumentation

The model used in the experiment was a 7° half-angle cone with an axial length of 40.64 cm and a base diameter of 9.96 cm. The cone is composed of a sharp nosetip, a roughness insert, and the main body. Three roughness inserts were used in the experiment. The inserts all span an axial distance of 3.81 to 6.35 cm from the nosetip.The first was a smooth insert (Roughness 0). The second insert had 50 dimples with a depth of 0.15 mm and a diameter of 0.20 mm equally spaced azimuthally around the entire insert at an axial distance of 5.08 cm from the nosetip (Roughness 1), and the third insert had the same number and configuration of dimples with a depth of 0.61 mm and a diameter of 0.76 mm (Roughness 2). The roughness inserts were used to introduce streamwise vorticity to be amplified by the stationary crossflow wave, allowing for greater control of the location where the stationary instability reaches saturation.

Nine sensor holes with a diameter of 3.2 mm were drilled perpendicular to the model surface to accommodate the installation of eight PCB132A31 (PCB) pressure sensors and one Medtherm Schmidt-Boelter (SB) heat transfer gauge. The SB gauge is located at axial distances of 27.4 cm from the nosetip and two arrays of four PCB pressure transducers are located at an axial distance of 36.8 and 38.1 cm. Each of the PCB transducers at a given axial distance are located at a 6° azimuthal angle pitch. See Figure 10 for a photo of the model and a table of sensor locations.

The PCB signals were recorded at a sampling rate of 5 MHz. The voltage data were separated into 0.1 second intervals for post-processing. This interval was chosen so that conditions would remain approximately constant for the duration of the run, based on the time that it takes for the expansion wave to travel the length of the driver tube. PSDs were calculated for the 0.1 second time intervals using Welch's method. The intervals were broken up into 2,500 windows of equal length, providing a frequency resolution of 2 kHz , with 50% percent overlap of each window. Pressure fluctuation data were normalized by the freestream pressure P_∞, which was calculated using isentropic relationships for compressible flow and the assumptions that $M_\infty = 6.0$ and $\gamma = 1.4$.

C. Secondary Instability Results

The secondary instability of the stationary crossflow wave should manifest as a frequency peak in the PSD plots at roughly 300 kHz, with growing amplitude along the axial direction of the cone. Figure 11 shows the PSD plot and TSP images for Re = 10.7×10^6/m with the roughness 2 element inserted into the model. In Figure 11(a) the PSD plots for the front sensor located at 126° and the back sensor located at 132° from the windward ray exhibit peaks in the PSD at roughly 300 kHz. Additionally, in Figure 11(b) the TSP
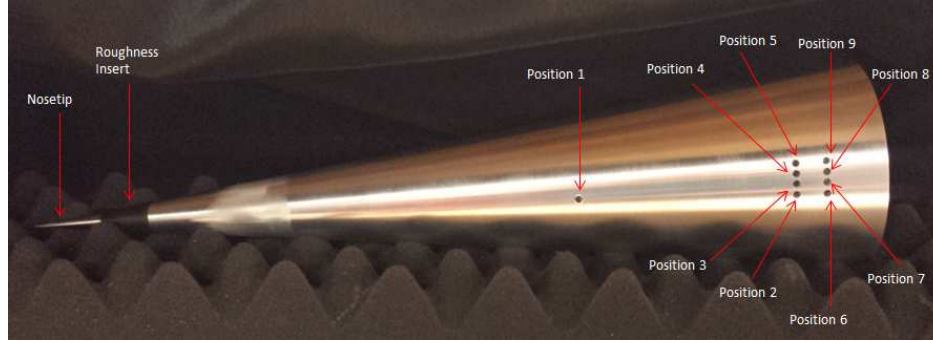
Sensor Position	Axial Location (cm)	Azimuthal Angle (°)	Sensor Type
1	27.4	3	SB
2	36.8	0	PCB
3	36.8	6	PCB
4	36.8	12	PCB
5	36.8	18	PCB
6	38.1	0	PCB
7	38.1	6	PCB
8	38.1	12	PCB
9	38.1	18	PCB

Figure 10. The 7° half-angle cone used for data collection, showing the nosetip, roughness insert, and nine sensor holes. Angles are measured with respect to sensor position 2.

image of the heat transfer shows that a more brightly colored streak, indicative of the heating caused by the stationary crossflow wave, appears to partially pass over both the front 126° sensor and the back 132° sensor. Figure 12(a) shows a comparison of the front 126° sensor and the back 132° sensor.

By observation of the peak in Figure 12(a), the frequency associated with the peak measured by the PCB in the front array at 126° was determined to be approximately 280 kHz. The frequency associated with the peak measured by the PCB in the back array at 132° was determined to approximately 310 kHz, roughly 10% greater than the frequency measured by the PCB in the front array. The amplitude of the peak in the PSD is larger at the back sensor than the front sensor, which is expected as the secondary instability of the stationary crossflow wave propagates downstream and grows. It should be noted that the peaks which are measured by the front and back PCBs at 138° exhibit the opposite behavior, where the amplitude of the peak decreases from the front to the back sensor, therefore these peaks are not examined further. The growth in peak amplitude could possibly explain the growth of the frequency associated with the peak as axial distance increases. However, since the change in frequency of the secondary instability with respect to axial distance is not known, it cannot be definitively determined that the observed data is from the secondary instability.

To determine if the frequencies associated with the peaks detected by the PCBs in the front array at 126° and the back array at 132° are from the same instability, the coherence was calculated. The square of the magnitude of the coherence, C_{xy}, is a measure of the correspondence of the two , assuming a linear transfer function between the two signals, at each frequency. The values of coherence range from 0 to 1, where 0 indicates that the two signals have no relation and 1 indicates perfect correlation, with values greater than 0.2 considered significant.[10] Figure 12(b) plots the magnitude-squared coherence as a function of frequency from the PSDs generated by the PCBs in the front array at 126° and the back array at 132°. A peak of magnitude around 0.35 is present around 300 kHz, suggesting that there is a correspondence between the signals being measured by the PCBs in each row. Furthermore, using the coherence plot a plot of the time
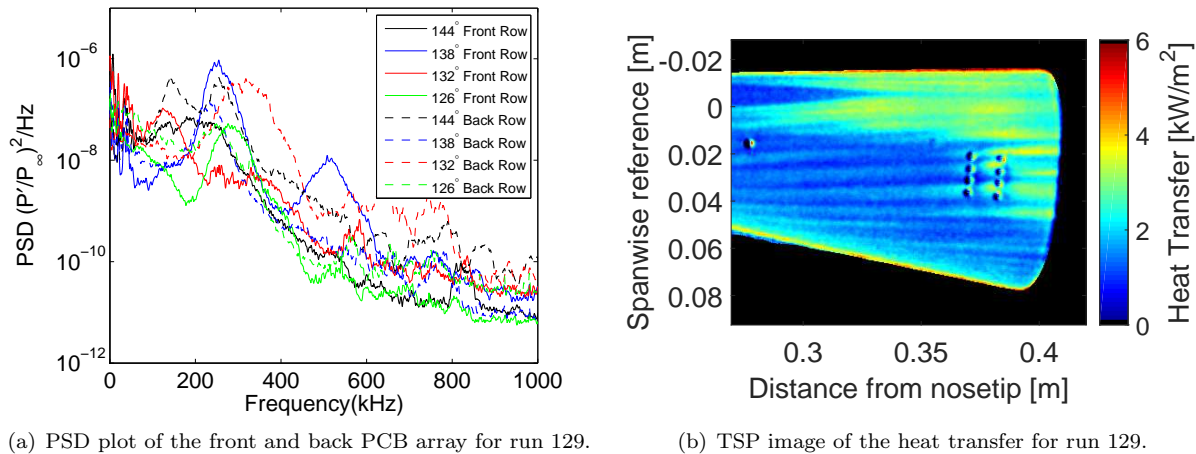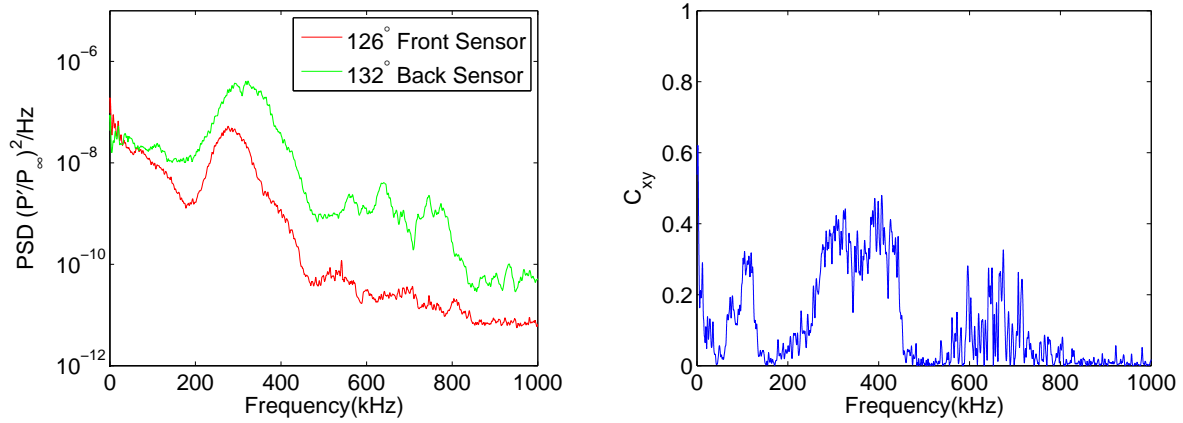
9

(a) PSD plot of the front and back PCB array for run 129.

(b) TSP image of the heat transfer for run 129.

Figure 11. Roughness 2, Re = 10.7×10⁶/m

lag between the signals was generated. As shown in Figure 12(c) it can be seen that in the region of interest around 300 kHz there is a nearly constant time lag of approximately 22 μs. For a sensor separation distance of 1.3 cm, this corresponds to a velocity of approximately 577 m/s, or roughly 28 % of the freestream velocity.

Data from a run with roughness 1, Re = 10.8×10⁶/m in Figure 13 also shows possible evidence of the secondary instability of the stationary crossflow wave. The sensors located at 138° in both the front and back rows in the PSD plot in Figure 13(a) show a frequency associated with the peak of approximately 335 kHz for the front sensor and near 320 kHz for the back sensor. Figure 14(a) plots the PSDs generated by the 138° front and back sensors. It can be seen that the amplitude of the peak in the PSD remains relatively constant as the flow moves downstream. The TSP image Figure 13(b) shows a streak indicative of a stationary crossflow vortex passing directly over the sensor pair. It is strongly believed that the measured frequency is that of the secondary instability. This correlates well with Henderson's findings for the 3° angle of attack cone, although the initial conditions are slightly different in this run. Additionally, Figure 14(b) shows a very large peak of around 0.70 in the magnitude-squared of the coherence for the two signals in the frequency range of 315 to 360 kHz. Furthermore, Figure 14(c) shows that in the region of interest around 300 kHz the time lag between the two signals is approximately constant around 15 μs. This corresponds to a velocity of approximately 846 m/s, or roughly 41 % of the freestream velocity.

An interesting note from the roughness 1 and the roughness 2 run is the difference in frequency associated with the peak shift from the front sensor to the back sensor. In the roughness 1 run the frequency associated with the peak decreased by about 20 kHz over the 1.27 cm distance between sensors, however, for the roughness 2 run the frequency associated with the peak increased by approximately 30 kHz. The only significant controlled difference between the two runs was the roughness element. If the assumption is made that all of the measurements resulted from the secondary instability, it is difficult to reconcile the variance in frequency. Based on the data, it appears that the frequency of the secondary instability decreases with increasing axial distance while maintaining approximately the same power level, until just before breakdown when the frequency and power both rise. This can be seen in Figure 15. These results show that further experiments are necessary to attempt to achieve consistent results for similar run conditions. Specifically, future experiments should take more care to properly shield the PCBs from ground loops and modify the angle of attack adapter to allow for more precise alteration of the azimuthal angle.

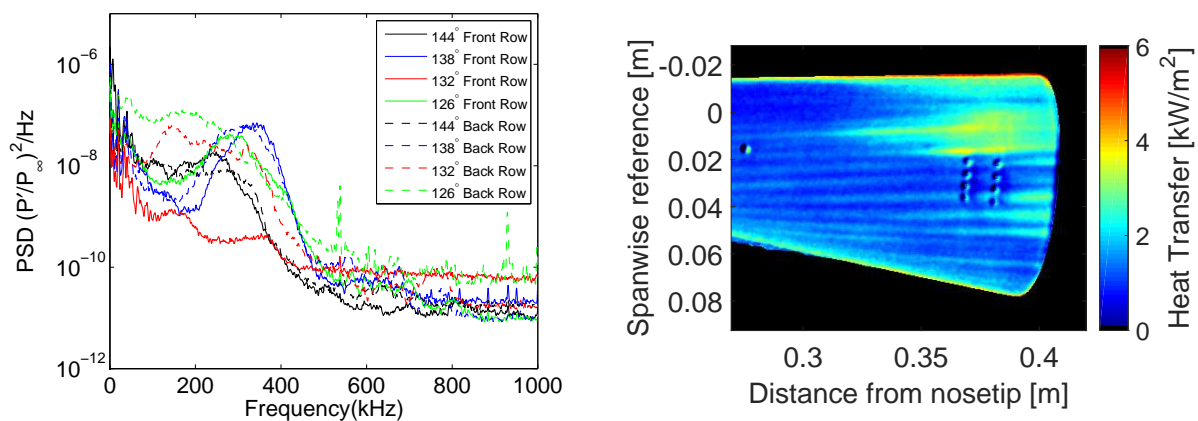errors on this page wrt % of freestream velocity.

10

(a) PSD plot of the front 126° and back 132° PCB sensors for run 129.

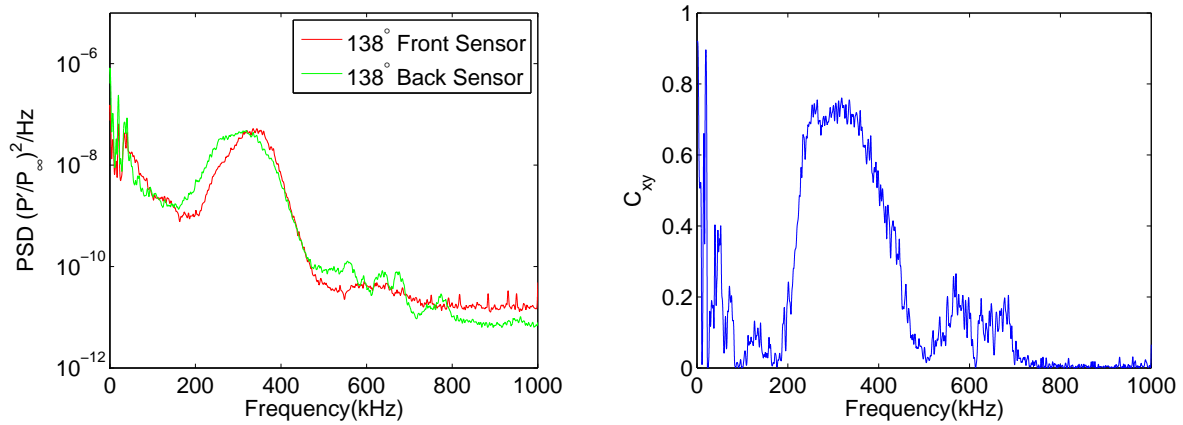(b) Square of the magnitude of the coherence for the signals from the front and back sensors.
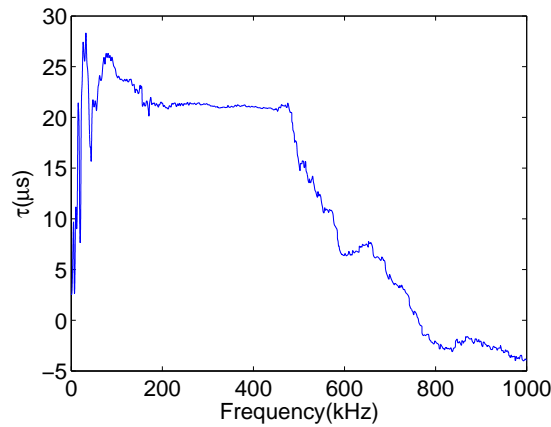
(c) Time lag for the signals from the front and back sensors.

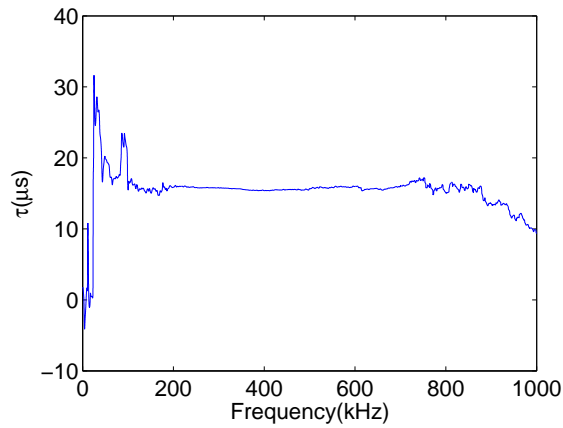**Figure 12. Front PCB sensor at 126° and back PCB sensor at 132°.**

(a) PSD plot of the front and back PCB array for run 123.

(b) TSP image of the heat transfer for run 123.

Figure 13. Roughness 1, Re $= 10.8 \times 10^6$/m

11

(a) PSD plot of the front 138° and back 138° PCB sensors for run 123.

(b) Square of the magnitude of the coherence for the signals from the front and back sensors.

(c) Time lag for the signals from the front and back sensors.

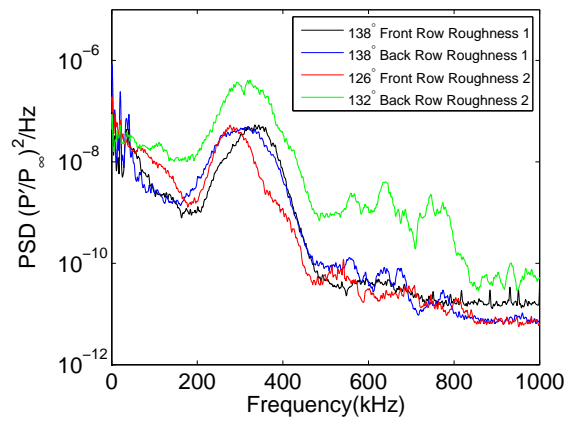**Figure 14. Front PCB sensor at 138° and back PCB sensor at 138°.**

Figure 15. PSD plots comparing runs 123 and 129.

12

IV.   Roughness and Air Jet Induced Transition on a Generic Hypersonic Forebody

It is desirable to have a turbulent boundary layer develop on the forebody of a scramjet. Large pressure gradients at compression corners and in the isolator could cause a laminar boundary layer to separate, potentially leading to engine unstart and loss of the vehicle. Antoine Durant from MBDA-France and Thierry André from the Institut de Combustion Aérothermique Réactivité et Environnement (ICARE) brought a generic scramjet forebody for testing in the BAM6QT. The model was designed to test the effectiveness of roughness elements and an air jet for tripping the boundary layer. Roughness elements and discrete air jets have been investigated for use as boundary layer trips for previous scramjet vehicles including Hyper-X and the X-51A.[11,12]

Pressure and TSP data for most inserts were collected at three angles of attack (0°, 2°, 4°) and several Reynolds numbers. Computations from ICARE are needed to help substantiate experimental data on wake instabilities. More information about the test and results is available in *Mach 6 Quiet tunnel Laminar to Turbulent investigation of a Generic Hypersonic Forebody*, to be presented at the 20th AIAA Space Planes and Hypersonic Systems Conference by Durant, *et al.* in July.

V.   Conclusion

1. A straight 3° half-angle cone was tested under quiet flow in the BAM6QT. Adjusting the model to zero angle of attack was not feasible using the set screws in the sting support. Even with this difficulty, natural transition was observed under quiet flow near the aft end of the model at a unit Reynolds of 12.1×10^6/m. The non-linear growth of the second-mode instability was measured. Maximum pressure fluctuation magnitudes prior to the onset of transition were measured to be 27% of the mean surface pressure.

2. Experiments searching for the secondary instability of the stationary crossflow wave were performed on a 7° half angle cone at 6° angle of attack. Using a newly designed sensor array consisting of eight PCB132A31 pressure transducers, further indications of the secondary instability were observed. For Reynolds numbers of approximately 10.7×10^6/m and azimuthal angles between 125° and 140° from the windward ray it is believed that the secondary instability was observed. However, further verification is required. Future experiments should take more care to properly shield the PCBs from ground loops, as well as modifying the angle of attack adapter so that the azimuthal angle of the PCBs can be more precisely adjusted.

VI.   Acknowledgements

References

[1]Schneider, S. P., "Developing Mechanism-Based Methods for Estimating Hypersonic Boundary-Layer Transition in Flight: The Role of Quiet Tunnels," *Progress in Aerospace Sciences*, Vol. 72, January 2015, pp. 17–29.

[2]Fujii, K., "Experiment of the Two-Dimensional Roughness Effect on Hypersonic Boundary-Layer Transition," *Journal of Spacecraft and Rockets*, Vol. 43, No. 4, July–August 2006.

[3]Marineau, E. C., Moraru, C. G., Lewis, D. R., Norris, J. D., Lafferty, J. F., and Johnson, H. B., "Investigation of Mach 10 Boundary Layer Stability of Sharp Cones at Angle-of-Attack, Part 1: Experiments," *AIAA Paper 2015-1737*, January 2015.

[4]Chynoweth, B. C., *A New Roughness Array for Controlling the Nonlinear Breakdown of Second-Mode Waves at Mach 6*, Master's thesis, Purdue University, School of Aeronautics and Astronautics, Expected August 2015.

[5]Willems, S., Gülhan, A., Ward, C. A., and Schneider, S. P., "Free Transition on a Slender Cone in a Quiet and a Conventional Wind Tunnel and the Effect of Ultrasonically Absorptive Materials," To Be Presented: 6th European Conference for Aeronautics and Space Sciences, June-July 2015.

[6]Helen L. Reed, W. S. S., "Stability and Transition of Three Dimensional Boundary Layers," *Annual Review of Fluid Mechanics*, Vol. 21, 1989, pp. 235–284.

[7]Mujeeb R. Malik, Fei Li, M. M. C. and Chang, C.-L., "Secondary Instability of Crossflow Vortices and Swept-Wing Boundary-Layer Transition," *Journal of Fluid Mechanics*, Vol. 399, 1999, pp. 85–115.

[8]Kohama, Y., "Some Expectations on the Mechanism of Cross-Flow Instability in a Swept-Wing Flow." *Acta Mechanica*, Vol. 66, February 1987, pp. 22–38.

[9]Poll, D. I. A., "Some Observations of the Transition Process on the Windward Face of Long Yawed Cylinder," *Journal of Fluid Mechanics*, Vol. 150, 1985, pp. 329–356.

[10]Christopher Ward, R. O. H. and Schneider, S. P., "Possible Secondary Instability of Stationary Crossflow Vortices on an Inclined Cone at Mach 6," To be published.

[11]Berry, S. A., Nowak, R. J., and Horvath, T. J., "Boundary Layer Control for Hypersonic Airbreathing Vehicles," *AIAA 2004-2246*, June 2004.

[12]Borg, M., *Laminar Instability and Transition on the X-51A*, Ph.D. thesis, Purdue University, West Lafayette, IN, July 2009.